Enamel Repair with Amorphous Ceramics

Yan Wei, Shaojia Liu, Zuohui Xiao, Hewei Zhao,* Jun Luo, Xuliang Deng,* and Lin Guo*

Developing high-performance materials in physiological conditions to clinically repair stiff tissue for long lifespan remains a great challenge. Here, an enamel repair strategy is reported by efficiently growing a biocompatible ZrO_2 ceramic layer on defective enamel through controllable hydrolysis of Zr^{4+} in oral-tolerable conditions. Detailed analysis of the grown layer indicates that the grown ZrO_2 ceramic is amorphous without grain boundary and dislocation, which endows the repaired enamel with natural enamel comparable mechanical performance (modulus ≈82.5 GPa and hardness ≈5.2 GPa). Besides, the strong chemical connection between unsaturated coordinated Zr^{4+} in amorphous structure and PO_4^{3-} greatly strengthen the crystalline–amorphous interface of the repaired enamel to endure the long-time mastication damage. Moreover, these ZrO_2 ceramics provide hydrophilic, electronegative, and smooth surfaces to resist the adhesion and proliferation of cariogenic bacteria. The hybrid amorphous–crystalline interface design with advantages in biomechanical compatibility would promote the evolution of a variety of cutting-edge functional materials for medical and engineering application.

Living creatures use ceramics as building blocks to assemble their hierarchical supporting architectures, from the outer shell of mollusk,[1,2] arthropods, and crustacean[3,4] to the endoskeletons of echinoderms[5,6] and vertebrates.[7,8] Understanding the evolutionary advantages of these bioceramics in terms of the mechanical characteristics has enabled the development of new load-bearing materials. Tooth enamel, which is composed of hyperminearlized hydroxyapatite (HA) crystals (96 wt%), is an exceptionally hard bioceramic and has the primary function of protecting oral physiology.[9,10] The important role of enamel is inevitably compromised by various pathological risks, such as cariogenic bacteria, mechanical insult, or beverages with extreme pH values, resulting in serious oral diseases and systemic disorders.[11] Although some enamels can achieve nano- to microscale self-recovery induced by hydration, such as giant panda,[12] but the superhard and highly crystallized tooth enamel of most vertebrates cannot be self-regenerated to restore both geometry and mechanical properties throughout the lifetime.[10] Developing reliable and sustainable enamel repair techniques would improve the life quality of living organisms and prolong the lifespan of bioceramic-inspired load-bearing materials.

In a clinical setting, synthetic materials comprising resins and glass-ion cements are most commonly used to top-down fill defective enamel,[13–17] but their polymerization shrinkage results in microleakage at the material-enamel interface.[13,14] There has been recent progress in bottom-up enamel repair technologies that are functionalized in some cases for HA remineralization,[15,16] HA nanoparticle assembly,[17] and bioinspired ceramic–polymer composites.[18] However, the inefficient mechanical recover and weak interfacial connection[19] of bottom-up repair with crystalline materials significantly compromised their capability to restore and protect teeth. Amorphous phases have recently been demonstrated to be a transient precursor in the biomineralization of many tissues, such as bones,[20–23] nacres,[24] and teeth,[25] some of which could even be maintained after biomineralization. In adult tooth enamel, the amorphous phase remains as the intergranular phase between HA nanorods, which renders the enamel with excellent mechanical properties and resistance to acid attack. The unique structure of amorphous materials, such as a lack of grain boundaries and dislocations,[26,27] isotropy[28] and large number of active sites, contributes to the outstanding mechanical performance of enamel.[25] However, in terms of enamel repair, almost all studies are focused on filling the defective region by hard artificial crystals or emulating the ordered

Prof. Y. Wei, Dr. Z. Xiao, Prof. X. Deng
Department of Geriatric Dentistry
NMPA Key Laboratory for Dental Materials
National Engineering Laboratory for Digital
and Material Technology of Stomatology
Beijing Laboratory of Biomedical Materials
Peking University School and Hospital of Stomatology
Beijing 100081, P. R. China
E-mail: kqdengxuliang@bjmu.edu.cn
Dr. S. Liu, Prof. H. Zhao, Prof. L. Guo
Beijing Advanced Innovation Center for Biomedical Engineering
School of Chemistry
Beihang University
Beijing 100191, P. R. China
E-mail: zhaohewei@buaa.edu.cn; guolin@buaa.edu.cn
Prof. J. Luo
Center for Electron Microscopy
Institute for New Energy Materials & Low-Carbon Technologies
School of Materials Science and Engineering
Tianjin University of Technology
Tianjin 300384, P. R. China

The ORCID identification number(s) for the author(s) of this article can be found under https://doi.org/10.1002/adma.201907067.
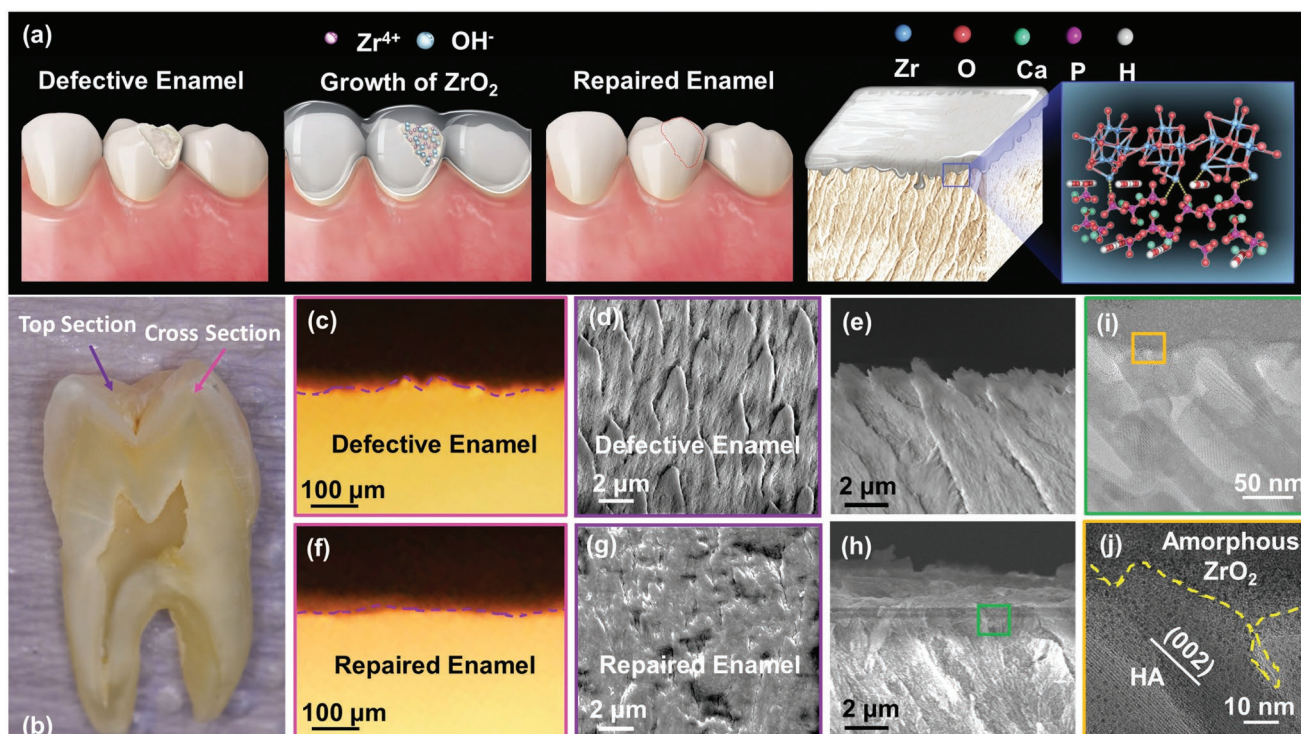
Figure 1. Fabrication and morphology of amorphous ZrO_2 layer-coated tooth enamel. a) Schematic illustration of the preparation and structure of the bionic repair of tooth enamel by the in situ growth of an amorphous ZrO_2 layer. b) Optical photograph of human enamel sample in which the purple arrow corresponds to the top section and the pink arrow corresponds to the cross section. c) Optical image of the acid-etched enamel (E-Acid etched) viewed from the cross section. d,e) SEM images of the E-Acid etched viewed from the top section (d) and cross section (e). f) Optical image of the amorphous ZrO_2 layer-coated enamel (E-Amorphous ZrO_2) viewed from the cross section. g,h) SEM images of the E-Amorphous ZrO_2 viewed from the top section (g) and cross section (h). i) TEM of cross-sectional view of E-Amorphous ZrO_2 in which the amorphous coating layer and the substrate enamel can be easily distinguished. j) HRTEM image taken from (i), showing that some amorphous ZrO_2 infiltrated into the gaps between the HA nanowires, which greatly enhanced the interfacial connection.

mineralized structure of the enamel, and the naturally occurring and beneficial amorphous phase has rarely been explored. Hence, the application of organized amorphous phases directly on to tooth enamel to optimize its repair is still an exciting and unattained goal.

Herein, through sequential nucleation, deposition and homogeneous layer growth, we develop a facile and efficient enamel repair strategy by the in situ growth of amorphous ZrO_2 ceramics. The repaired tooth enamel shows a high modulus of ≈82.5 GPa and a hardness of ≈5.2 GPa, which are comparable to those of sound enamel and 2.4 and 2.0 times higher than those of acid-etched enamel, respectively. This synthetic approach could also significantly increase the interfacial connection by interfiling amorphous ZrO_2 to the gaps between HA nanowires as well as taking advantages of the large number of active sites in amorphous ZrO_2 to form chemical connection in the crystalline–amorphous interface. Furthermore, the in situ grown ZrO_2 could provide a hydrophilic, electronegative and smooth surface to resist the adhesion and proliferation of cariogenic bacteria. This strategy for designing mechanically compatible interfacial materials could be extended to other high-performance load-bearing materials for application in a variety of fields.

Defective tooth enamel specimens were obtained by slicing back human teeth along the direction perpendicular to the

enamel column (Figure S1, Supporting Information) and subsequently using orthophosphoric acid (35%) to etch them. As illustrated in **Figure 1**a, the defective enamel were repaired by in situ growing ZrO_2 ceramic layer on enamel through sequential processes of ions absorption, nucleation and heterogeneous growth along the enamel directed by the LaMer's law.[29] The key of the in situ growth of ZrO_2 layer is the balance between metal ions' heterogeneous growth and nucleation during hydrolysis, which was realized by adjusting the pH in the reaction system through using buffer solution and tuning the reaction temperature to guarantee the formation of a layer on the surface of the enamel instead of particle packing (Figure 1a). Details of the synthetic process and potential clinical application can be seen in the Experimental Section. The morphology of the acid-etched enamel (E-Acid etched) and amorphous ZrO_2 layer coated enamel (E-Amorphous ZrO_2; The amorphous phase of the coating layer was demonstrated by X-ray diffraction (XRD) (Figure S2, Supporting Information), which showed no diffraction peaks for ZrO_2 synthesized following the same strategy without enamel and showed no additive diffraction peaks for the E-Amorphous ZrO_2.) were characterized by scanning electron microscopy (SEM), transmission electron microscopy (TEM) and optical microscopy (OM) from the top and cross section as illustrated in Figure 1b. For E-Acid etched sample, the enamel edge is rough (Figure 1c) and the

ADVANCED
SCIENCE NEWS

www.advancedsciencenews.com

ADVANCED
MATERIALS

www.advmat.de

HA nanowires were easily distinguished in the uneven surface of the E-Acid etched sample with distinct dents and defects from both the top (Figure 1d) and cross-sectional (Figure 1e) views owing to the corrosion of HA nanowires, which sharply decreased the density of the HA packing, while the E-Sound was uniform and dense (Figure S3, Supporting Information). After repair, the surface roughness of E-Amorphous ZrO_2 was clearly reduced (Figure 1f) and the surface was dense and flat with no obvious cracks (Figure 1g and Figure S4, Supporting Information) from top sectional view, which means that the ZrO_2 coating was intact. The mean square roughness of the E-Amorphous ZrO_2 was ≈48.2 nm (Figure S5 and Table S1, Supporting Information), which was as smooth as that of the sound enamel (E-Sound, 43.4 nm, Figure S5 and Table S1, Supporting Information) and two times smoother than that of E-Acid etched sample (90.8 nm, Figure S5 and Table S1, Supporting Information), which is consistent with the phenomenon observed by OM and SEM. From the cross-sectional view, the amorphous layer coating can be easily distinguished from the enamel (Figure 1h,i), which had a thickness of ≈400 nm (Figure 1h and Figure S6, Supporting Information) and closely connected to the enamel. Energy dispersive spectroscopy (EDS) maps from the top surface (Figure S7, Supporting Information) clearly show that Zr elements were evenly dispersed in the E-Amorphous ZrO_2, which further demonstrates the formation of ZrO_2. It is worth noting that some amorphous ZrO_2 infiltrated seamlessly into the gaps between the HA nanowires (Figure 1j), which promote the contact area in the interface and form physical occlusion (Figure 1j) to enhance the interfacial connection. Furthermore, the E-Amorphous ZrO_2 was co-cultured with human gingival fibroblasts (HGFs), which showed the same trends in cell proliferation, morphology and adhesion to the other enamel surfaces, including surface of sound enamel, acid etched enamel and remineralized enamel (Figure S8, Supporting Information), verifying a good biocompatibility of the amorphous ZrO_2 layer.

In addition to the physical permeation between the amorphous ZrO_2 and E-Acid etched sample, the chemical state of the interface between the enamel and coating was also investigated with Raman spectroscopy (Figure S9, Supporting Information) and Fourier transform infrared spectroscopy (FTIR) (Figure S10, Supporting Information). Two additive peaks in the Raman spectrum were discovered when the Raman spectrum of tooth enamel (Figure S9, Supporting Information) in the range of 200–300 cm^{-1}, where the peaks were due to ZrO_2[30] which confirms the formation of ZrO_2 (Figure S9, Supporting Information). Moreover, the characteristic peaks of HA in the amorphous ZrO_2 were extremely wide, which indicated a strong chemical interaction between the enamel and confirmed that the amorphous ZrO_2 coating was amorphous. In addition, the characteristic signal of PO_4^{3-}[31] of E-Amorphous ZrO_2 had a redshift in the FTIR spectra compared with E-Acid etched (Figure S10, Supporting Information), which indicated that the coordination between Zr^{4+} and PO_4^{3-} to improve the connection between the coated ceramic layer and the substrate enamel (schematic illustration in Figure 1a).

The coated amorphous ZrO_2 layer not only enabled the E-Acid etched sample to obtain a dense architecture similar to that of the E-Sound sample but also allowed the E-Acid etched sample to recover its mechanical performance, including both the Young's modulus and hardness. Quasistatic nanoindentation was conducted to obtain the stiffness of the E-Sound, E-Acid etched, E-Amorphous ZrO_2, and E-Remineralized enamel (E-Remineralized) samples as a comparison, as shown in Figure S11 (Supporting Information). The typical loading-unloading curves with the same limited load (100 mN) and using Berkovich indenters are plotted in **Figure 2**a, and the parallel nanoindentations were carried out at least four times (Figure S12, Supporting Information). It should be noticed that the contact depth obtained in the nanoindentation test for E-Amorphous ZrO_2 is above 1000 nm, which involves the coated ZrO_2 layer and the substrate enamel, so the mechanical properties discussed below is the hybrid mechanical performance of the repaired enamel. The Young's modulus and hardness were calculated by the Oliver-Pharr method,[32] as shown in Figure S9 (Supporting Information). Obviously, the modulus (90.1 GPa) and hardness (6.0 GPa) of the E-Sound sample dropped sharply to 34.5 and 2.6 GPa, respectively (Figure S13, Supporting Information), after acid pickling. When an amorphous ZrO_2 layer was coated, the modulus and hardness of the E-Amorphous ZrO_2 recovered to 82.5 and 5.2 GPa, respectively, which is 2.4 times and 2.0 times higher than those of E-Acid etched sample, respectively, and comparable to the E-Sound sample (Figure S13, Supporting Information), indicating excellent mechanical recovery. As a comparison, a commercial resin, Clearfil AP-X, was used to repair the E-Acid etched sample, whose modulus and hardness were 15.8 and 1.0 GPa, respectively (Figure S14 and Table S2, Supporting Information); these values are much lower than those of the E-Amorphous ZrO_2. Compared to the enamel obtained by remineralization, E-Remineralized only achieved a slight recovery in the modulus (from 34.5 to 40.7 GPa), while the hardness was even lower than that of the E-Acid etched sample, as the structure of the remineralized layer was relatively loose (Figure S11, Supporting Information). To investigate the uniformity of the Young's modulus (E_Y) and hardness (H), typical distribution maps of E_Y and H were constructed and excellent mechanical properties were obtained in the 0.25 mm × 0.25 mm matrix. This result further indicated the effective mechanical performance and resilience on a large scale due to the enamel repair with amorphous ZrO_2 (Figure 2b,c and Figure S15, Supporting Information), which is consistent with the quasi static nanomechanical properties. In addition, the dynamic mechanical properties, including storage modulus (E') and damping coefficient (tan δ), were studied (Figure 2d,e). The value of E' for the E-Amorphous ZrO_2 (68.5 GPa) was comparable to that of the E-Sound sample (≈78.4 GPa). The tan δ of the E-Amorphous ZrO_2 (0.06) was even higher than that of the E-Sound sample (0.05), which indicated that E-Amorphous ZrO_2 had a greater ability to resist the continuous external pressure and protect the inner layer of the enamel.

Several mechanisms are proposed herein to explain the excellent mechanical recovery due to the in situ growth of the amorphous ZrO_2 layer. The nanoindentation zones after indentation with a Berkovich indenter were analyzed for the E-Sound, E-Acid etched, E-Amorphous ZrO_2, and E-Remineralized samples with SEM (Figure 2f–h). The permanent deformation zones for all four enamels showed a quadrahedron-like morphology
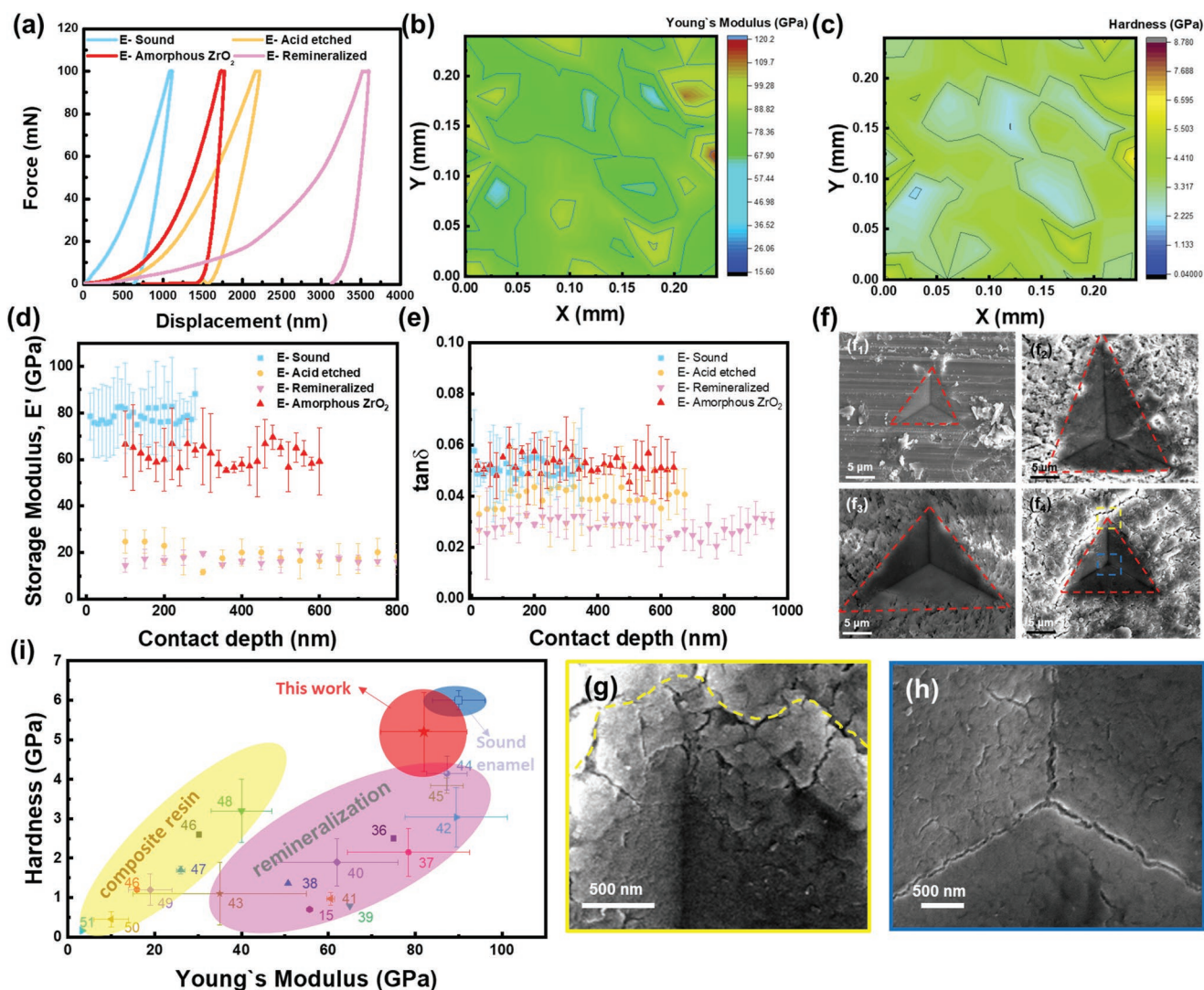
Figure 2. Mechanical performance of different enamels. a) Load–displacement curves tested by quasistatic nanoindentation of different enamels, including E-Sound, E-Acid etched, E-Amorphous ZrO_2, and remineralized enamel (E-Remineralized) samples. Quasistatic nanoindentation tests for the typical contour maps of the b) Young's modulus and c) hardness of the E-Amorphous ZrO_2. d,e) Nanoscale dynamic mechanical analysis (Nano-DMA) nanoindentation test of storage modulus (E') (d) and damping coefficient (tan δ) (e) of different enamels. f) Permanent deformation zone of different enamels after nanoindentation: f_1) E-Sound, f_2) E-Acid etched, f_3) E-Remineralized, and f_4) E-Amorphous ZrO_2, demonstrating that the permanent deformation area of E-Amorphous ZrO_2 and E-Sound were similar and low compared to E-Acid etched and E-Remineralized, meaning that they were stiff. g,h) Detailed observation of the permanent deformation zone of E-Amorphous ZrO_2 taken from (f4). i) Comparison of mechanical properties among composite resin repaired, remineralization repaired, and our in situ grown amorphous ZrO_2 repaired.

(Figure 2f₁–f₄), while the area of the permanent deformation zone varied. The E-Sound sample and E-Amorphous ZrO_2 had similar areas and were the smallest among the tested samples (Figure 2f₁,f₄), whereas the permanent deformation of both the E-Acid etched (Figure 2f₂) and E-Remineralized samples (Figure 2f₃) were 1.5 times larger than those of the other samples. The smaller the permanent deformation zone was, the higher the modulus and hardness of enamel were, which matches the results of the nanoindentation test (Figure 2a). For the E-Sound sample, the parallel HA nanowires were dense and stiff,[25] so a brittle fracture occurred at the edge of the indentation zone to dissipate energy (Figure S16a, Supporting Information). Similarly, the E-Amorphous ZrO_2 also dissipated the external load by warping at the edge (Figure 2g) owing to the

stiffness and densification provided by the amorphous layer. In comparison, the corrosion of the HA in the E-Acid etched sample and loose structures in the E-Remineralized sample made them too weak to bear an external load, and several scallops were generated by the partial collapse of the enamel architecture during indentation. In addition, many microcracks occurred during the indentation in both the E-Sound (Figure S16b, Supporting Information) and E-Amorphous ZrO_2 (Figure 2h) samples, which dissipated extra stress and suppressed permanent deformation, further preventing the sudden collapse of the HA-nanowire-based structure. In regard to the E-Acid etched (Figure S17, Supporting Information) and E-Remineralized samples (Figure S18, Supporting Information), similar microcracks were not observed but many holes

were generated by the collapse of the loose structure. Surprisingly, cracks in the E-Amorphous ZrO_2 near the indenter tip propagated preferentially along a wavy path (Figure 2h), which can dissipate energy just like the toughening behavior in a tooth enamel;[33–35] this behavior helped the E-Amorphous ZrO_2 achieve an improved viscoelasticity, which inhibited brittle fracture of the enamel, allowed it to bear a continuous external pressure, and even surpassed the viscoelasticity of the E-Sound sample (Figure 2e). In addition, the amorphous state of the ZrO_2 layer also contributed to an excellent mechanical recovery, as amorphous materials are continuous and lack grain boundaries and dislocations compared to a crystal.[27]

When compared to traditional enamel repair methods, our enamel repair with amorphous ceramics is outstanding (Figure 2i). Both the Young's modulus and hardness of E-Amorphous ZrO_2 surpassed the values of enamel repaired by remineralization[15,36–45] and with a composite resin,[46–51] which showed a similar behavior to the E-Sound samples (Figure 2i). To the best of our knowledge, the adoption of amorphous ZrO_2 in the fields of enamel repair has not been previously reported, and our enamel repair approach has been proven advantages, indicating great potential for future clinical applications.

In addition to the mechanical performance recovery, adhesion between the coated amorphous layer and the substrate enamel is also vital to evaluate whether their use is feasible. Here, a nanoscratch test was carried out (**Figure 3**a) to investigate the interfacial adhesion strength of the repair layer under a certain penetration depth of the indenter (350 nm) and subsequent 5 µm horizontal movement (Figure S19, Supporting Information). The lateral force versus time curves obtained from the nanoscratch test are plotted in Figure 3b. The critical lateral force for crack initiation (Lc1) and coating
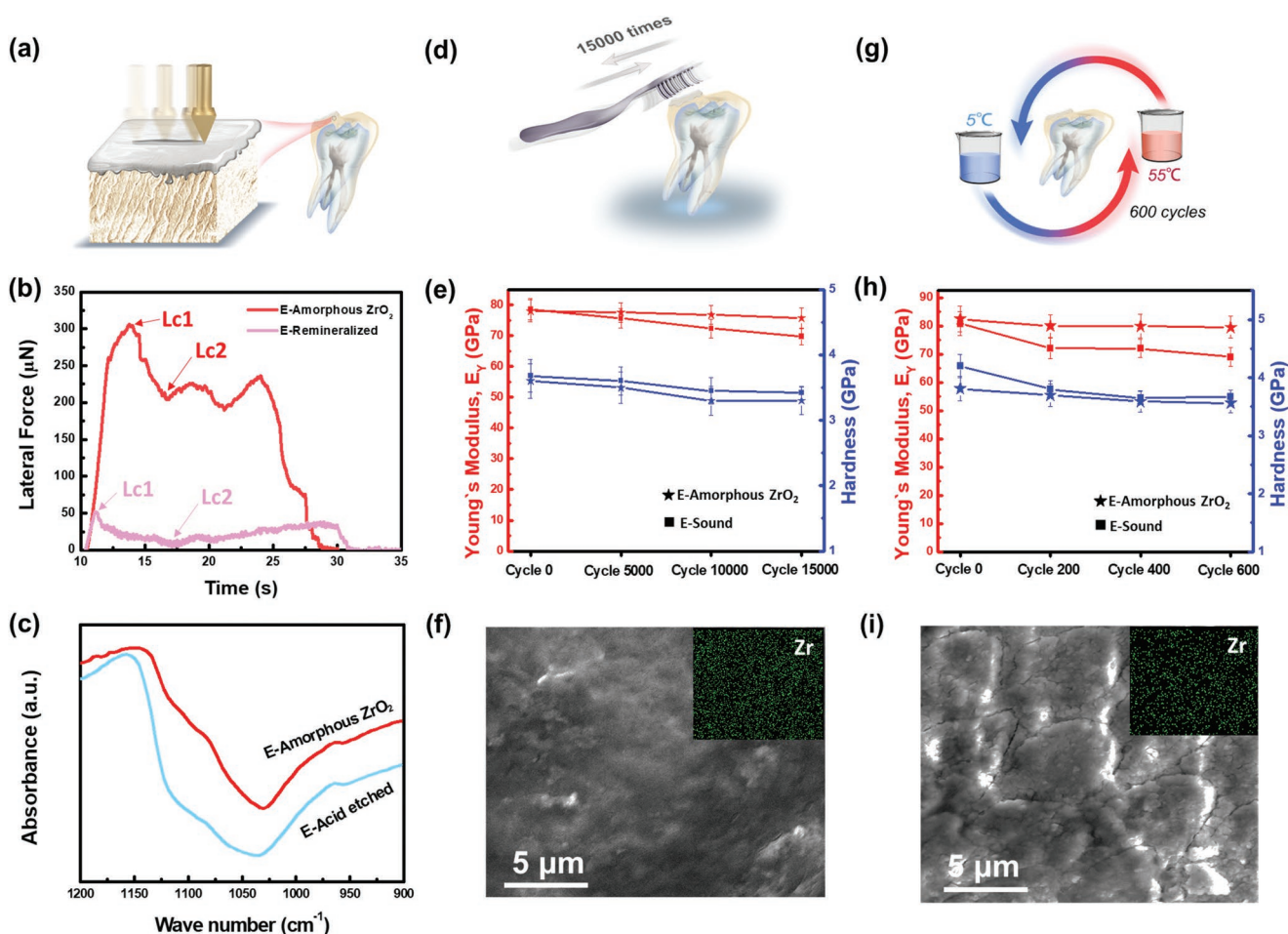

Figure 3. Strong interface connectivity and stability of amorphous ZrO_2 repaired enamels. a) A schematic of nanoscratch testing. b) Lateral force–time curves for E-Amorphous ZrO_2 and E-Remineralized sample, showing that a lateral force six times higher is needed to scratch the coated amorphous layer on the E-Amorphous ZrO_2. c) The infrared (IR) characteristic absorption peak of E-Amorphous ZrO_2 attributed to PO_4^{3-} had a significant redshift compared with the E-Acid etched sample. d) A schematic of the toothbrush experiment. e) Young's modulus and hardness of E-Amorphous ZrO_2 and E-Sound sample before and after 15 000 times toothbrush passes. f) SEM image of the repaired enamel after 15 000 times toothbrushing, where the amorphous ZrO_2 repaired layer exists uniformly on the enamel surface. g) A schematic of thermocycling testing. h) Young's modulus and hardness of E-Amorphous ZrO_2 and E-Sound sample before and after 600 times thermocycling. i) SEM image of the repaired enamel after 600 times thermocycling. Similarly, through the thermocycling experimental process, the mechanical properties of the E-Amorphous ZrO_2 and E-Sound can be maintained, and the amorphous ZrO_2 restoration layer covered the enamel surface perfectly. Overall, our method is effective and provides endurance for restored enamel.

slicing (Lc2) were observed at two clear transition points (Figure 3b). The Lc1 of the E-Amorphous ZrO_2 reached 310 µN, whereas the E-Remineralized sample showed an Lc1 of 52 µN, which is 6 times lower (Figure 3b). With the indenter horizontally scratching, the lateral force for the E-Amorphous ZrO_2 was waved around ≈230 µN, the decreasing of which can be attributed to slight slicing of the coatings. As a comparison, the lateral force for the E-Remineralized decreased to below 10 µN during the scratching, which means that the remineralized layer was weak connected and delaminated. Along with the FTIR signal from the E-Amorphous ZrO_2 (Figure 3c), it should be noted that the characteristic peak of PO_4^{3-} had an obvious redshift compared with E-Acid etched (≈1035 cm^{-1} shift to 1025 cm^{-1}), which suggested the coordination between Zr^{4+} and PO_4^{3-}. The difficulty scratching the E-Amorphous ZrO_2 means that the coated amorphous layer had a strong adhesion to the enamel, which is consistent with the physical permeation and strong chemical connection mentioned above. In addition, the remineralized layer could be detached within 10 s by using a simple ultrasonic treatment, while the coated amorphous ZrO_2 layer remained stable even after ultrasonic treatment for 10 min, which further qualitatively demonstrated the strong adhesion between the enamel and our *in-situ* grown amorphous ZrO_2 layer.

When considering inevitable normal abrasion, such as toothbrushing, and cold-hot stimulation-induced separation, the stability and persistence of the repair layer in an oral environment influences the enamel repair effects. Therefore, the wear resistance of the E-Amorphous ZrO_2 and the adhesion properties of the amorphous ZrO_2 repair layer were investigated by toothbrushing and thermocycling tests, and the simulation experiment process is shown in the Figure 3d–g, respectively. Thanks to the strong adhesion between the repair layer and the enamel, the decrease in the Young's modulus and hardness of E-the Amorphous ZrO_2 was minimal (8% and 6%, respectively) after 15 000 toothbrushing passes, which simulated toothbrushing for one year. The changes in the Young's modulus and hardness of E-the Amorphous ZrO_2 were even smaller than those of the E-Sound (15% and 10%, respectively) (Figure 3e), indicating that the coated amorphous layer exhibited a better ability to resist daily toothbrushing abrasion. The amorphous ZrO_2 layer was uniformly maintained on the enamel surface after toothbrushing (Figure 3f, detail of the middle process can be seen in Figure S20, Supporting Information); its morphology was similar to that of the enamel before the toothbrush experiment (Figure S16a, Supporting Information), further demonstrating the high abrasion resistance for E-Amorphous ZrO_2. Similarly, the mechanical properties, including both the modulus and hardness, decreased slightly for E-Amorphous ZrO_2 after thermocycling 600 times (3% and 2%, respectively, Figure 3h), and these values were smaller than the modulus and hardness decreases for the E-Sound sample (8% and 7%, respectively). The surface of the thermocycled E-Amorphous surface was still fully covered by a dense and uniform amorphous ZrO_2 coating (Figure 3i, details of the middle process can be seen in Figure S21, Supporting Information). The high resistance of the E-Amorphous ZrO_2 to both toothbrushing and thermocycling treatment described above proved that our repair approach was effective and provided durability for the restored enamel, thus bridging scientific research with practical applications.

Early colonization of carious bacteria, such as *Streptococcus mutans*, can not only produce acid to demineralize tooth but also provide the ligand binding sites for subsequent plaque formation.[52] The antibacterial activities of the as-achieved surfaces against S. mutans were investigated using SEM. As shown by the pseudo-morphological image analysis in **Figure 4**a, bacteria adhered and proliferated on all these surfaces after 1 h owing to their biocompatibility. After 6 h of culture, the lowest amount of bacteria were observed on the E-Amorphous ZrO_2 surface, while the surfaces of E-Sound, E-Acid etched and E-Remineralized samples were almost fully covered by bacteria (Figure 4b). This trend was confirmed by a quantitative evaluation using the viable cell count method (Figure 4d). Compared to the E-Sound, E-Acid etched and E-Remineralized samples, the amount of *S. mutans* on the E-Amorphous ZrO_2 surface was reduced by more than 10^5 per square millimeter after 6 h of culture. After 12 h, large amounts of *S. mutans* were colonized on these surfaces, which made it difficult to count single cells. Therefore, using 3D tomographic scanning techniques in confocal laser scanning microscopy (CLSM), we compared the immuno-fluorescence intensity of bacterial plaques after live/dead staining (Figure 4c). Only loose plaque was observed on the E-Amorphous ZrO_2, while compact plaque was formed on the E-Sound, E-Acid etched and E-Remineralized surfaces. Moreover, significant differences were found in the surface coverage percentages of bacteria (Figure 4e). The area covered by bacteria on the E-Amorphous ZrO_2 was at least 50% less than that of the other sample groups, which indicated that the E-Amorphous ZrO_2 surface had the slowest bacterial proliferation. These results suggested that the E-Amorphous ZrO_2 surface presented a strong resistance to bacterial adhesion and proliferation, which is in agreement with previous reports.[53] To determine the underlying mechanism, we characterized the physiochemical properties of these surfaces. The amorphous ZrO_2 layer was found to completely recover the low surface roughness (Figure 1 and Table S1, Supporting Information) and surface electric potential of the enamel (Table S1, Supporting Information). In contrast, acid etching and remineralization significantly increased the surface roughness and surface electric potential of the enamel, and these factors have been demonstrated to facilitate bacterial adhesion. Furthermore, E-Amorphous ZrO_2 achieved the highest hydrophilicity among these surfaces considered in this study according to the water contact angle (WCA) test (E-Amorphous ZrO_2 (30.7°) < E-Remineralized (34.7°) < E-Acid etched (58.8°) < E-Sound (62.4°)) (Figure S22, Supporting Information). Previous studies illustrated that the surface hydration and the steric hindrance effects from high hydrophilicity could prevent the adsorption of protein on the enamel surface and therefore eliminate the adhesion of bacteria.[54] Thus, the amorphous ZrO_2 layer could not only recover but also optimize the antibacterial adhesion and proliferation properties of enamel to a substantial degree.

In summary, we developed a novel approach to repair enamel by the in situ growth of an amorphous ZrO_2 layer by controlling the balance between nucleation and growth of ZrO_2. Until now,
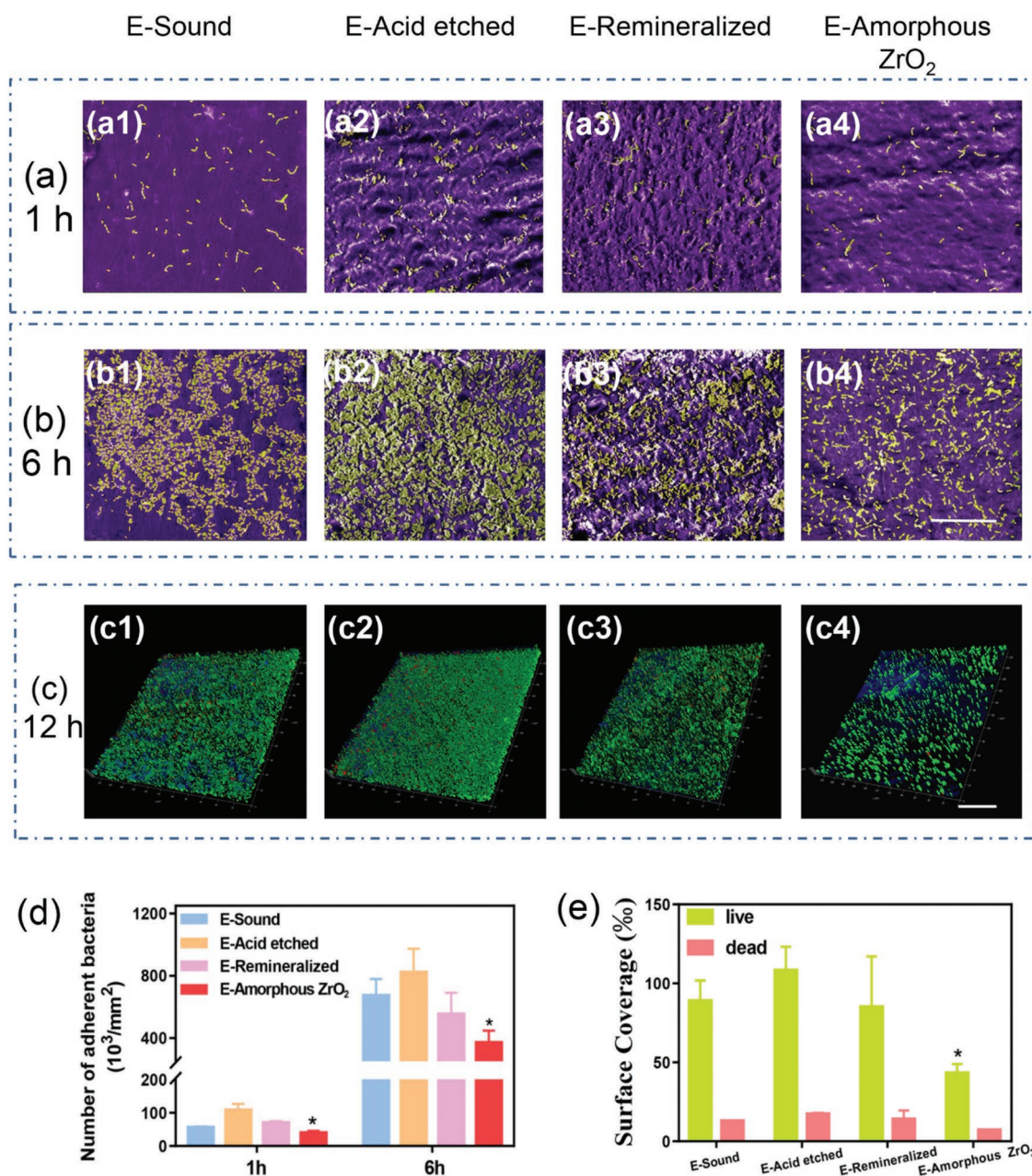
Figure 4. The amorphous zirconia layer showed excellent antibacterial adhesion and proliferation capability. a,b) Representative pseudo-morphological images from SEM after 1 and 6 h of bacterial culture, indicating the least amount of *S. mutans* on the E-Amorphous enamel surface (a1,b1: E-Sound; a2,b2: E-Acid etched; a3,b3: E-Remineralized; and a4,b4: E-Amorphous ZrO_2. Scale bars: 15 µm). d) Quantitative analysis showing the significantly highest antibacterial adhesion and proliferation ratio on the E-Amorphous enamel surface (*$p < 0.05$). c) 3D tomographic confocal laser scanning microscopy (CLSM) images of the live/dead assay after 12 h of bacterial culture, demonstrating that only loose plaque was observed on E-Amorphous enamel, while compact plaque was formed on E-Sound, E-Acid etched, and E-Remineralized surfaces (Scale bars: 50 µm). e) Fluorescence area analysis indicated that the bacteria covered area on E-Amorphous enamel was at least 50% less than those in the other groups.

there is no report about using amorphous ceramics to restore defective enamel. The recovered enamel exhibited a comparable modulus (82.5 GPa) and hardness (5.2 GPa) to those of the sound enamel, which was ≈2.4 times and ≈2.0 times higher than those of the defective enamel, respectively. In addition, the coated amorphous layer showed strong adhesion to the enamel owing to the existence of strong interfacial chemical bonding, whose mastication damage resilience is even better than the sound enamel. Furthermore, the restored enamel presented strong resistance to bacterial adhesion and proliferation, providing basis for living health. We proposed a general strategy for clinical stiff tissue repair through amorphous–crystalline interface design, which could be extended to construct high-performance load-bearing materials in the future.

Experimental Section

Sample Preparation: Human erupted third molars were collected from patients aged between 18 and 40 years at Stomatology Hospital of Peking University after signing written informed consent. Teeth without caries, fluorosis, cracking, or other defects were required. Enamel blocks (≈3 mm × 3 mm × 2 mm) sawed from the buccal and lingual tooth surfaces were first polished with 800- to 5000-grit SiC paper, and a small window area (2 mm × 2 mm) in the center of each enamel surface was defined as the reaction area. Enamel blocks without any treatment were sonicated for 5 min and classified into the sound enamel (E-Sound) group. A 35% phosphoric acid gel (Gluma, Heraeus Kulzer, Hanau, Germany) was coated for 20 s on the enamel surface to prepare demineralization blocks in the E-Acid etched group. The samples were then washed with sterile Milli-Q water for 60 s, sonicated again for 5 min, and stored at 4 °C in sterile Milli-Q water prior to use. Ethical approval was obtained from the Institutional Review Board (IRB) of Peking University Hospital of Stomatology (No. PKUSSIRB-201951174).

Preparation of Amorphous ZrO_2 Coated Enamel: Here, the amorphous ZrO_2 layer was in situ grown on the acid etched enamel. In a typical synthesis, a tris(hydroxymethyl)aminomethane-hydrochloric acid buffer solution with pH ≈ 7.5 was prepared by dispersing 0.848 g tris(hydroxymethyl)aminomethane and 475 μL concentrated hydrochloric acid in 70 mL deionized water. Then, the acid etched enamel was immersed in the buffer solution and subsequently cooled to 10 °C by cold bath. After that, the $ZrOCl_2 \cdot 8H_2O$ (14 mg) was added and the solution was incubated at 10 °C for 3 h under vigorously stirring. It should be noted that the 4–12 °C is acceptable for the growth process and the stirring is not prerequisite. Next, the enamel was collected after carefully washed with deionized water to clean out remnant salt and subsequently dried in air for 10 min. Finally, the dried enamel was solvothermal treated with ethyl alcohol at 80 °C for 12 h to dehydrate the coated layer and obtain the amorphous ZrO_2 layer coated enamel.

For potential application of the ZrO_2 growing strategy, a suitable custom tray will be first fabricated by using the patient's tooth as model so that only the defective region has space after the patient wearing the custom tray. Second, the reaction solution (precooled) can be injected to the space between defective region and the custom tray, and a small and suitable ice bag can be adhered to the custom tray to keep a low temperature of the space. After finish of the growth process, the custom tray will be got off and the enamel will be washed by water. Finally, the custom tray will be worn again and injected with ethyl alcohol, which will be subsequently heated by laser, a mature technology in current oral treatment. It should be noted that the reaction time can be divided to several treatments according to the patients' oral condition.

Remineralization Treatment: Casein phosphopeptide–amorphous calcium phosphate (CPP-ACP) was applied for remineralization therapy as a control. The CPP-ACP product Tooth Mousse Plus (GC Corporation, Japan) was bought and remineralized on the E-Acid etched blocks. A sufficient amount of CPP-ACP paste was laid over on the reaction areas using disposable microapplicators (TPC, Advanced Technology, USA) repeatedly for 10 min once every 12 h for 5 d and immersed in simulated saliva at room temperature.

Morphology Characterization: The surface and cross-section structures of different enamels, including E-Sound, E-Acid etched, E-Amorphous ZrO_2, and E-Remineralized, were obtained by environmental scanning electron microscopy (ESEM) (Quanta 250F, FEI), and nanoindentation zones were observed by SEM (7500F, JEOL). EDS maps were taken along with the SEM images. TEM characterizations were carried out on JEOL 2010F with 200 kV and the specimens were cut by the Focused Ion beam (FIB, Helios NanoLab 460HP). The different enamel surface roughnesses were reviewed using atomic force microscopy (AFM) (Bruker Dimension Icon), where enamel specimens were pasted on steel disks.

Phase Characterization: XRD (XRD-6000, Shimadzu) was carried out to explore the phase structures of the amorphous ZrO_2, E-Sound, and E-Amorphous ZrO_2 with Cu Kα radiation. The scan range was 20°–80°, and the scan rate was 5° min^{-1}. All samples were placed on glass.

Spectroscopy Characterization: Raman spectroscopy measurements were obtained by LabRAM HR800 (Horiba JobinYvon) with an incident laser having a wavelength of 633 nm He-Ne laser line at room temperature. The laser power density was ≈109 W m^{-2} (laser power: ≈1.5 mW; laser spot: 1.87 μm^2). FTIR spectra were collected using a Thermo Nicolet nexus-470 FTIR instrument. Before the measurement, the background of IR spectrum was recorded by testing black silicon. Then, the whole enamel blocks was placed on silicon wafer and transferred into the infrared detection area. The spectra were collected at a 2 cm^{-1} resolution and averaged over 64 scans.

Nanoindentation Test: The mechanical properties characterization, including Young's modulus and hardness of the E-Sound, E-Acid etched, E-Amorphous ZrO_2, and E-Remineralized samples, were measured in ambient conditions (25 °C, 20% RH) using a commercial TI950 triboindenter (Hysitron) equipped with a Berkovich diamond tip ($R \approx 100$ nm) by a continuous depth-sensing indentation technique. For the standard load, the initial depth of 10 nm, terminational depth of 500 nm, and loading rate of 10 nm s^{-1} were applied. For the high load, the limited force and load time were set at 100 mN and 20 s, respectively. To investigate the mechanical properties of different contact depths, the initial depth was 20 nm, the final depth was 2000 nm, and the interval of displacement was 20 nm. For the quasistatic nanoindentation, Young's modulus and nanohardness were calculated following the methods of Oliver-Pharr. Nanodynamic mechanical analyses (nanoDMA measurements) were performed with the same triboindenter with the specialized program of NanoDMA and the Berkovich tip. The following data are presented as they were provided by the Sample Analysis Report from Hysitron, Inc. (2009). Typically, the load function was set with an initial quasistatic force of 20 μN and a peak quasistatic force of 10 000 μN, the frequency and dynamic force were 45 Hz and 30 μN, respectively.

Nanoscratch Experiment: The nanoscratch experiments were performed using the tip to obtain frictional forces and the adhesive strength of the interface between the E-Amorphous ZrO_2 layer (or remineralization layer) and enamel. The scratch was operated by increasing the contact depth of 0–100 nm and 0–350 nm for 20 s first, and then the horizontal slip length was 5 μm (time: 10–30 s) for each test.

Toothbrushing Wear Test: Enamel blocks were fixed to the surface of each sample bench by a self-curing resin to reach the same exposure height. A 200 g load was delivered by soft toothbrushes (Oral-B Indicator 35 Toothbrush, Short Head, UK), and all test samples were immersed in a slurry of toothpaste (Oral-B Pro-Health, Procter & Gamble) solution that comprised 16 g of toothpaste with 100 mL of deionized water. The specimens were submitted to a total of 15 000 reciprocal strokes (60 cycles min^{-1}) of toothbrushing (Custom-made machine according to ISO/TR 14569-1:2007(E)), which corresponded to ≈1 year of toothbrushing wear. After the 5000, 10 000, and 15 000 stroke mechanical wearing tests were finished, the enamel blocks were taken apart from the resin for SEM observation and nanoindentation tests.

Thermocycling Test: Before the thermocycling test, the samples were packed in gauze and placed in a stainless steel basket. The basket was immersed and subjected to thermocycling for 600 cycles at temperatures alternating between 5 and 55 °C with an immersion time of 90 s (PolyScience, USA). The transfer time between baths was 5 s. All specimens exposed to thermocycling were kept in deionized water at room temperature. During the 200, 400, and 600 cycling tests, the samples were removed for SEM observation and nanoindentation tests.

Bacterial Adhesion Test: *S. mutans* (ATCC 25175) was purchased from the China General Microbiological Culture Collection Center and cultured in brain-heart infusion (BHI) medium (Sigma-Aldrich, St. Louis, MO, USA). Enamel blocks from four groups were immersed in distilled water, placed in a 5 mL test tube and subjected to Co 60 radiation sterilization. For the bacterial adhesion testing, the enamel blocks were placed in 48-well plates and pretreated with artificial saliva (A7990, Solarbio, China) for 30 min at 37 °C to mimic the natural oral condition. The optical density of *S. mutans* at 530 nm (OD630) was adjusted to 0.02 (≈1 × 107 CFU mL^{-1}), and a 400 μL volume of bacterial suspension was

placed onto each enamel surface. To quantify the bacteria adhering to the enamel blocks, samples were removed from the bacterial suspension and rinsed with phosphate buffered solution (PBS) three times. Enamel blocks cultured with *S. mutans* at 37 °C for ≈1 and 4 h were fixed in 2.5% glutaraldehyde solution, rinsed with distilled water, dehydrated in a graded series of ethanol solutions (50%, 60%, 70%, 80%, 90%, and 100%) for 15 min, and then observed with SEM. Adherent cells in nine randomly selected 5000-fold magnification fields were counted, and the number of bacteria in 1 mm^2 was calculated. After being cultured in the bacterial suspensions for 12 h, the antibacterial activity was examined by the live/dead assay kit (Invitrogen, Singapore) for 15 min under no light conditions and was then observed by CLSM (Carl Zeiss, Jena, Germany). The fluorescence intensity area of layers from 3D images was calculated using Image Pro Plus 6.0.

Bacterial Adhesion-related Surface Property Tests: To further examine the properties related to bacterial adhesion, enamel blocks from four groups were studied with AFM, WCA and surface zeta (ζ) potential techniques. Samples were fixed on the center of the slide and detected by the AFM tip with a rectangular area of 2.5 μm^2. The WCA was measured by a Kruss DSC100 (Germany) by a drop of 2 μL on each enamel. The surface ζ potential was determined with a Zeta Sizer Nano-ZS Instrument (Malvern Instruments, Worcestershire WR, UK) in an aqueous environment at room temperature. Samples were cut into a rectangle with a length of 4 mm and a width of 3 mm and stuck to the test box on the reverse side.

Statistical Methods: Statistical analysis was performed with SPSS v.22.0 software (IBM, Armonk, NY, USA). Differences between groups were evaluated by one-way ANOVA with the LSD *t*-test. A $p < 0.05$ was considered statistically significant.

Supporting Information

Supporting Information is available from the Wiley Online Library or from the author.

Acknowledgements

Conflict of Interest

The authors declare no conflict of interest.

Keywords

[1] G. Mayer, *Science* **2005**, *310*, 1144.
[2] U. G. Wegst, H. Bai, E. Saiz, A. P. Tomsia, R. O. Ritchie, *Nat. Mater.* **2015**, *14*, 23.
[3] M. E. McNamara, D. E. Briggs, P. J. Orr, H. Noh, H. Cao, *Proc. R. Soc. London, Ser. B* **2011**, *279*, 1114.
[4] S. Perkins, *Science* **2015**, *349*, 1431.
[5] C. Moureaux, J. Simon, G. Mannaerts, A. I. Catarino, P. Pernet, P. Dubois, *Aquat. Toxicol.* **2011**, *105*, 698.
[6] J. N. Weber, E. W. White, J. Lebiedzik, *Nature* **1971**, *233*, 337.
[7] J. Y. Rho, L. K. Spearing, P. Zioupos, *Med. Eng. Phys.* **1992**, *20*, 92.
[8] C. A. Webster, D. Di Silvio, A. Devarajan, P. Bigini, E. Micotti, C. Giudice, M. Salmona, G. N. Wheeler, V. Sherwood, F. B. Bombelli, *Nanomedicine* **2016**, *11*, 643.
[9] B. Yeom, T. Sain, N. Lacevic, D. Bukharina, S.-H. Cha, A. M. Waas, E. M. Arruda, N. A. Kotov, *Nature* **2017**, *543*, 95.
[10] J. L. Cuya, A. B. Manna, K. J. Livi, M. F. Teaford, T. P. Weihs, *Arch. Oral Biol.* **2002**, *47*, 281.
[11] L. H. He, M. V. Swain, *J. Mech. Behav. Biomed. Mater.* **2008**, *1*, 18.
[12] Z. Liu, Z. Weng, Z. F. Zhai, N. Huang, Z. J. Zhang, J. Tan, C. Jiang, D. Jiao, G. Tan, J. Zhang, X. Jiang, Z. Zhang, R. O. Ritchie, *Acta Biomater.* **2018**, *81*, 267.
[13] S. I. Ramoglu, T. Uysal, M. Ulker, H. Ertas, *Angle Orthod.* **2009**, *79*, 138.
[14] S. Langhorst, J. O'Donnell, D. Skrtic, *Dent. Mater.* **2009**, *25*, 884.
[15] Z. Xiao, K. Que, H. Wang, R. An, Z. Chen, Z. Qiu, M. Lin, J. Song, J. Yang, D. Lu, *Dent. Mater.* **2017**, *33*, 1217.
[16] Y. Liu, L. Tjäderhane, L. Breschi, A. Mazzoni, N. Li, J. Mao, D. H. Pashley, F. Tay, *J. Dent. Res.* **2011**, *90*, 953.
[17] L. Li, C. Mao, J. Wang, X. Xu, H. Pan, Y. Deng, X. Gu, R. Tang, *Adv. Mater.* **2011**, *23*, 4695.
[18] G. Tan, J. Zhang, L. Zheng, D. Jiao, Z. Liu, Z. Zhang, R. O. Ritchie, *Adv. Mater.* **2019**, *31*, 1904603.
[19] N. Moszner, U. Salz, J. Zimmermann, *Dent. Mater.* **2005**, *21*, 895.
[20] A. Lotsari, A. K. Rajasekharan, M. Halvarsson, M. Andersson, *Nat. Commun.* **2018**, *9*, 4170.
[21] J. Mahamid, A. Sharir, L. Addadi, S. Weiner, *Proc. Natl. Acad. Sci. USA* **2008**, *105*, 12748.
[22] X. Wang, H. C. Schröder, W. E. Müller, *J. Mater. Chem. B* **2018**, *6*, 2385.
[23] V. Čadež, I. Erceg, A. Selmani, D. Domazet Jurašin, S. Šegota, D. Lyons, D. Kralj, M. Sikirić, *Crystals* **2018**, *8*, 254.
[24] A. Rao, T. Roncal-Herrero, E. Schmid, M. Drechsler, M. Scheffner, D. Gebauer, R. Kröger, H. Cölfen, *ACS Cent. Sci.* **2019**, *5*, 357.
[25] L. M. Gordon, M. J. Cohen, K. W. MacRenaris, J. D. Pasteris, T. Seda, D. Joester, *Science* **2015**, *347*, 746.
[26] H. Zhao, Y. Yue, Y. Zhang, L. Li, L. Guo, *Adv. Mater.* **2016**, *28*, 2037.
[27] F. Li, H. Zhao, Y. Yue, Z. Yang, Y. Zhang, L. Guo, *ACS Nano* **2019**, *13*, 4191.
[28] G. Kumar, H. X. Tang, J. Schroers, *Nature* **2009**, *457*, 868.
[29] H. Zhao, Y. Zhu, F. Li, R. Hao, S. Wang, L. Guo, *Angew. Chem., Int. Ed.* **2017**, *56*, 8766.
[30] S. Koutsopoulos, *J. Biomed. Mater. Res.* **2002**, *62*, 600.
[31] S. Mansour, S. El-Dek, M. Ahmed, *Sci. Rep.* **2017**, *7*, 43202.
[32] G. Pharr, A. Bolshakov, *J. Mater. Res.* **2002**, *17*, 2660.
[33] Z. Liu, Z. Zhang, R. O. Ritchie, *Adv. Mater.* **2018**, *30*, 1705220.
[34] D. Bajaj, D. D. Arola, *Biomaterials* **2009**, *30*, 4037.
[35] Z. Y. Weng, Z. Q. Liu, R. O. Ritchie, D. Jiao, D. S. Li, H. L. Wu, L. H. Deng, Z. F. Zhang, *J. Mech. Behav. Biomed. Mater.* **2016**, *64*, 125.
[36] L. Zheng, J. Zheng, Y. Zhang, L. Qian, Z. Zhou, *J. Phys. D: Appl. Phys.* **2013**, *46*, 404006.
[37] Y. Cao, M. L. Mei, Q.-L. Li, E. C. M. Lo, C. H. Chu, *J. Dent.* **2014**, *42*, 1535.
[38] H.-Y. Chung, C. C. Li, *Mater. Sci. Eng., C* **2013**, *33*, 969.
[39] C. Hsu, H. Chung, J.-M. Yang, W. Shi, B. Wu, *J. Dent. Res.* **2011**, *90*, 88.
[40] H. Wang, Z. Xiao, J. Yang, D. Lu, A. Kishen, Y. Li, Z. Chen, K. Que, Q. Zhang, X. Deng, *Sci. Rep.* **2017**, *7*, 40701.

[41] M. Sun, N. Wu, H. Chen, *Sci. Rep.* **2017**, *7*, 9611.

[42] Y. Cao, M. L. Mei, Q.-L. Li, E. C. M. Lo, C. H. Chu, *ACS Appl. Mater. Interfaces* **2014**, *6*, 410.

[43] S. Elsharkawy, M. Al-Jawad, M. F. Pantano, E. Tejeda-Montes, K. Mehta, H. Jamal, S. Agarwal, K. Shuturminska, A. Rice, N. V. Tarakina, *Nat. Commun.* **2018**, *9*, 2145.

[44] Y. Zhou, Y. Zhou, L. Gao, C. Wu, J. Chang, *J. Mater. Chem. B* **2018**, *6*, 844.

[45] C. Shao, B. Jin, Z. Mu, H. Lu, Y. Zhao, Z. Wu, L. Yan, Z. Zhang, Y. Zhou, H. Pan, *Sci. Adv.* **2019**, *5*, eaaw9569.

[46] R. A. Sfalcin, A. B. Correr, L. R. Morbidelli, T. G. F. Araújo, V. P. Feitosa, L. Correr-Sobrinho, T. F. Watson, S. Sauro, *Clin. Oral Invest.* **2017**, *21*, 2143.

[47] X. Wang, G. Huyang, S. V. Palagummi, X. Liu, D. Skrtic, C. Beauchamp, R. Bowen, J. Sun, *Dent. Mater.* **2018**, *34*, 228.

[48] H. Nezhad, V. Thakur, *Polymers* **2018**, *10*, 1106.

[49] S. El-Safty, R. Akhtar, N. Silikas, D. Watts, *Dent. Mater.* **2012**, *28*, 1292.

[50] J. L. Drummond, *J. Biomed. Mater. Res., Part B* **2006**, *78*, 27.

[51] Y. Issa, D. C. Watts, D. Boyd, R. B. Price, *Dent. Mater.* **2016**, *32*, 535.

[52] R. Gibbons, *J. Dent. Res.* **1984**, *63*, 378.

[53] S. L. Aktuğ, S. Durdu, E. Yalçın, K. Çavuşoğlu, M. Usta, *Mater. Sci. Eng., C* **2017**, *71*, 1020.

[54] A. Almaguer-Flores, P. Silva-Bermudez, R. Galicia, S. E. Rodil, *Mater. Sci. Eng., C* **2015**, *57*, 88.